HHS Public Access

Author manuscript

IEEE Trans Med Imaging. Author manuscript; available in PMC 2018 October 01.

Published in final edited form as:

IEEE Trans Med Imaging. 2017 October ; 36(10): 2171–2178. doi:10.1109/TMI.2017.2723479.

Intravascular Ultrasound Imaging with Virtual Source Synthetic Aperture (VSSA) focusing and Coherence Factor Weighting (CFW)

Mingyue Yu[+],
Department of Biomedical Engineering and USC Roski Eye Institute, Los Angeles, CA 90089 USA

Yang Li[+],
Department of Biomedical Engineering, Los Angeles, CA 90089 USA

Teng Ma[*],
Department of Biomedical Engineering and USC Roski Eye Institute, Los Angeles, CA 90089 USA, and Institute of Biomedical and Health Engineering, Shenzhen Institutes of Advanced Technology, Chinese Academy of Sciences, Shenzhen 518055, China

K. Kirk Shung, and
Department of Biomedical Engineering, Los Angeles, CA 90089 USA

Qifa Zhou[*]
Department of Biomedical Engineering and USC Roski Eye Institute, Los Angeles, CA 90089 USA

Abstract

Intravascular ultrasound (IVUS) has been frequently used for coronary artery imaging clinically. More importantly, IVUS is the fundamental image modality for most advanced multimodality intravascular imaging techniques since it provides a more comprehensive picture of vessel anatomy on which other imaging data can be superimposed. However, image quality in the deeper region is poor because of the downgraded lateral resolution and contrast-to-noise ratio. In this study, we report on the application of an ultrasound beamforming method that combines virtual source synthetic aperture (VSSA) focusing and coherence factor weighting (CFW) to improve the IVUS image quality. The natural focal point of conventional IVUS transducer was treated as a virtual source that emits spherical waves within a certain region. Mono-static synthetic aperture focusing was conducted to achieve higher resolution. Coherence factor was calculated using delayed RF signals and applied to the synthesized beam to increase the contrast-to-noise ratio (CNR) and focusing quality. The proposed method was tested through simulations in Field II and imaging experiments in both linear and rotational scans. The lateral resolution for linear scan mode is improved from 165–524 μm to 126–143μm; resolution for rotational scan mode improves by up to 42%. CNR improvement by up to 1.5 was observed on the anechoic cysts of different sizes and at different locations. Herein, it is demonstrated that the beamforming method which

[*]Teng Ma and Qifa Zhou are the corresponding authors for this work (tengma@usc.edu and qifazhou@usc.edu).
[+]Mingyue Yu and Yang Li contribute equally in this work.

combines VSSA and CFW can significantly improve the IVUS imaging quality. This approach can be readily integrated into the current IVUS imaging system for enhanced clinical diagnosis.

Index Terms

intravascular ultrasound (IVUS) imaging; ultrasound; ultrasonic imaging; virtual source synthetic aperture

I. Introduction

Cardiovascular disease (CVD) has been the No.1 killer in the United States, accounting for around 30.8% of all deaths. Coronary heart disease (CHD) alone contributes to 1 in every 7 deaths [1]. Atherosclerotic plaques build up gradually within the vessel wall of the coronary artery, which may remain asymptomatic until the high-risk plaques rupture suddenly and trigger subsequent thrombosis. This acute event typically results in coronary attack or even sudden death. Intravascular ultrasound (IVUS) imaging is the most frequently used coronary artery imaging tool for visualizing lumen dimension and the whole plaque volume clinically. IVUS can guide percutaneous coronary intervention (PCI), assist stent selection and placement, and assess stent deployment to predict later events [2]. With a better understanding of the pathological progression of atherosclerosis, vulnerable plaques, especially thin-cap fibroatheromas (TCFAs), containing a thin fibrous cap less than 65 um, are gaining more and more attention[3]. However, IVUS imaging alone cannot accurately detect the vulnerable plaques due to insufficient resolution and limited soft tissue contrast, which brings multimodality imaging for intravascular application onto the stage.

In recent years, several multimodality intravascular imaging techniques have been proposed to provide complementary information onto IVUS image for more comprehensive characterization of atherosclerosis. Integrated IVUS and optical coherence tomography (OCT) imaging [4–6], and multi-frequency IVUS imaging [7] [8] were proposed to identify thin fibrous cap utilizing high resolution information from OCT or high frequency IVUS. Integrated IVUS and near-infrared spectroscopy (NIRS) imaging [9, 10], integrated IVUS and intravascular photoacoustic (IVPA) imaging [11, 12], and integrated IVUS, OCT and Fluorescence imaging [13, 14] are developed to characterize the chemical composition of the plaque. Integrated IVUS and contrast-enhanced imaging [15, 16] has also been studied to monitor the *vasa vasorum* proliferation. It can be seen that in most of these innovative multimodality intravascular imaging technologies, IVUS remains indispensible because of its capability to evaluate plaque burden and monitor artery remodeling [14, 17] [18].

As a widely recognized clinical tool for intravascular imaging and the irreplaceable technical basis of most multimodality intravascular imaging techniques, however, IVUS itself still requires further improvement in the overall performance including spatial resolution and contrast-to-noise ratio (CNR) over the whole range of interest. Several approaches that have been reported to improve the IVUS image quality are illustrated in Fig. 1 by simulating the two-way beam pattern of single element IVUS transducers with a 0.5mm active aperture size in PZFlex (Weidlinger Associates, Cupertino, CA). Fig. 1(a) shows the two-way beam pattern of a conventional flat 40MHz IVUS transducer that is naturally focused at 1.7 mm.

Increasing the operational frequency of IVUS provides better spatial resolution within limited depth while sacrificing the CNR, and penetration depth of IVUS images beyond that depth [7]. The radiation pattern of a flat 80MHz IVUS transducer is shown in Fig. 1(b). It can provide good resolution at 3–4mm, but the intensity is significantly attenuated beyond the natural focus, causing degradation in CNR.

Mechanical focusing of the IVUS transducer is another approach to achieve higher resolution within the focus region [19]. The beam pattern of a 40MHz IVUS transducer with a mechanical focus at 3mm is presented in Fig. 1(c). Since the mechanical focal point of 3 mm is beyond the natural focal point of 1.7 mm, further mechanical focusing will only pull the focal zone towards the transducer surface, which will in turn decrease the sensitivity and lateral resolution in the rest of field of view (FOV) [19]. As shown in Fig. 1(c), narrow beam width can be achieved at 1–2mm, but the beam diverges beyond that region, where more artery structure information lies. Moreover, it is practically very challenging to geometrically focus the transducer of very small aperture size (e.g. 0.5mm×0.5mm).

Given the fact that increasing the center frequency and mechanical focusing method could only improve the lateral resolution and enhance the CNR within a certain region of FOV while downgrading the image quality outside of the focal region, it requires an accurate alignment between the focal zone of IVUS transducer and the region of interest. However, it is unrealizable to precisely control the exact position of the IVUS catheter inside the coronary artery with various lumen sizes in an actual intravascular imaging environment. In this scenario, a feasible image processing approach that will not downgrade with depth would be invaluable. Therefore, in this study, we applied an image processing method that can enhance the image quality of single element IVUS transducer over the entire FOV.

Synthetic aperture focusing technique based on virtual source concept was first proposed by Passman and Ermert to improve the image quality of strongly focused transducer [20]. The virtual source concept (VSSA) focusing was further studied [21, 22] [23] and extended to array transducers. Synthetic aperture sequential beamforming (SASB) was developed based on the virtual source concept for array transducers to produce high resolution ultrasound image at a high speed and at the same time massively reduce data load for different imaging applications [24] [25] [26] [27]. Based on the assumption that the focal region can be seen as the virtual source of a spherical wave within a certain angular range, VSSA focusing method can increase lateral resolution and extend imaging depth by combining adjacent scanlines that contain information of the synthesized line[20] [28] [29]. This inspires us to apply VSSA to the mechanical-state IVUS imaging for improving lateral resolution and SNR.

Even though the VSSA focusing method improves the resolution by synthesizing a large aperture, it brings in higher sibelobes, which can cause unwanted artifact [21] [30]. Amplitude apodization applied on the received data can suppress the sidelobe level and increase contrast resolution but broadening the mainlobe, or sacrificing lateral resolution [21]. Coherence factor based on the coherence of delayed RF signal has been used as a focusing criterion to quantitatively evaluate the image quality [31] [32]. Higher coherence factor value indicates delayed RF signals are more coherent among each other. It has been demonstrated that weighting the delayed beams adaptively using the coherent factor can

reduce the sidelobe level of the VSSA focused radiation pattern [33] and to further improve the resolution [28]. This method is called coherence factor weighting (CFW). The expected −6dB beamwidth contour after VSSA-CFW processing is illustrated by the green dash dot line in Fig. 1(d). The application of this combined method to conventional IVUS transducer has not yet been investigated.

In this study, the VSSA-CFW beamforming method was the first time extended to IVUS application for improving lateral resolution and CNR through the whole FOV. The applicability of this VSSA-CFW method was first demonstrated through simulations in Field II [34]. Then the efficacy was explored experimentally on tungsten wire phantom imaging, homogeneous agar-based phantom imaging, anechoic cyst phantom imaging and *ex vivo* human artery imaging. Both simulated and experimental results of wire target imaging demonstrate improvements in lateral resolution. CNR improvement is also clearly shown in the anechoic cyst phantom images. Image depth extension was quantitatively measured through in vitro imaging of the homogeneous phantom. In the human artery image, extended image depth, and better layer definition are achieved after image processing. To the best of our knowledge, this is the first time VSSA-CFW being used for IVUS imaging. This image processing method can be integrated into a current imaging system to improve the image quality of current IVUS imaging catheters. Moreover, it can further refine the multimodality intravascular imaging techniques to provide more accurate and comprehensive information for vulnerable plaque identification.

II. Method

A. Virtual Source Synthetic Aperture and Coherent Factor Weighting

In traditional B-mode imaging, where a single emission is used to acquire the information along the axial direction, the underlying assumption is that the acoustic field of the transducer is a narrow and uniform ‘pencil’ shape. In fact, the narrowest beamwidth is only achieved at the focal point; in the out-of-focus region, the resolution is inversely proportional to the distance from the focal point because of the beam divergence. This concept is illustrated in Fig. 2(a), where the shape of the transducer and beam profile are delineated with dashed line.

In the virtual source synthetic aperture (VSSA) focusing method, the focal point of the transducer is considered as a virtual source, as shown in Fig. 2(b), which produces a spherical wave within a limited angular range [21] [22]. The beam convergence and divergence before and after the focal point are simplified into two cone shapes, and the spreading angle α can be approximately determined by the $F_{\#}$ of the transducer using (1) and (2):

$$\alpha = 2arctan\left(\frac{1}{2F_{\#}}\right), \quad (1)$$

$$F_{\#}=\frac{Z_f}{D}, \quad (2)$$

where z_f is the focal depth of the transducer and D is the size of active aperture [29]. In rotating single-element based IVUS imaging, the transducer element undergoes rotational pullback motion, which combines the rotational scanning along the azimuthal direction in the cross-sectional view and linear scanning along the elevational direction in the longitudinal view. The cardiologists rely on the information from both cross-sectional view and longitudinal view to make an accurate diagnosis. Therefore, in this study, we applied the proposed method in both linear and rotational scan mode with single element IVUS transducer. We added two modifications to perform VSSA processing for an IVUS transducer. First, the natural focus was treated as the virtual source. The natural focal depth f_n is calculated using (3).

$$f_n={D^2}\big/{4\lambda}, \quad (3)$$

Second, instead of assuming an infinitely small focal point, the −3dB beamwidth region near the natural focus was considered during VSSA focusing. In the region surrounding the natural focal point, if the adjacent image point at the same depth is covered within the −3dB beamwidth region, the corresponding RF signal will be used for aperture synthesis using (4) and (5).

For linear scan imaging, mono-static VSSA utilizes the superimposed acoustic field from scan lines adjacent to each other, and combines echoes from different emissions to rebuild high-resolution image. For an imaging point target in the overlapping acoustic field, denoted as the green point in Fig. 2(b), VSSA focusing is done by delaying and summing the echo signals from adjacent emissions, whose beam field covers the imaging point, as shown in (5). The time delay is determined by the two-way propagation distance from the virtual source to the imaging point using (4) [33].

$$\Delta t_i=2sgn\,(z-f_n)\,\frac{[abs\,(z-f_n)-r]}{c} \quad (4)$$

$$S_{VSSA}(\mathrm{t})=\sum_{i=1}^{N}RF\,(i,,t-\Delta t_i) \quad (5)$$

where z is the depth of the imaging point, f_n is natural focal depth, r is the distance from the focal point to the imaging point. N is the number of scan lines used for aperture synthesis, labeled by the number in Fig. 2(b). N is determined by the spreading angle α, scanning step

size, and imaging depth. It should be noted that the delay is negative if the imaging point is before the focal point (closer to the transducer surface). The assumption of a virtual source/detector is based on the fact that the acoustic beams from the transducer surface add coherently at the focus. Therefore the time delay is calculated relative to the virtual source, instead of the transducer surface [21, 33]. Theoretical deduction of the method is outlined by Passmann and Ermert in their study [20].

For rotational scan imaging, the beamforming theory of VSSA is the same to linear scan, but the beam profile and aperture synthesis have to be considered in the polar coordinates instead of the Cartesian coordinates. As shown in Fig. 2(c), during the rotational scanning, the position of the transducer surface changes along a circular path. The radius of circular path r is determined by the size of the imaging probe. The angular step size during the rotation, beam spreading angle, and imaging depth, together determine the number of scan lines that can be used for beam synthesis, as represented by N in (5). Different from the linear scan situation, the beam overlap decreases with increasing depth during the rotational scan. Accordingly, N is not balanced before and after the focal point because of the beam separation during rotation. The received RF data was first passed through a 4th order Butterworth filter with a passband of 20–60MHz. Then VSSA focusing was done on the filtered data using (4) and (5). The VSSA-Only image was formed using S_{VSSA} in (5) through envelope detection and logarithmic compression.

In addition to the VSSA, coherent factor weighting (CFW) was applied to the synthesized beam S_{VSSA} in (5) to further improve focusing quality and contrast resolution [28] [33] [35, 36]. The coherence factor was calculated based on the signal coherence of delayed RF signals involved in the synthesized beam as indicated in (6). The coherence factor equals 1 when the delayed RF signals are perfectly coherent. It falls to 0 in the case of zero-mean random noise, or when the delayed signals are completely misaligned with each other. Therefore, the CFW method is capable of suppressing the sidelobes arose from VSSA focusing while further narrowing the mainlobe. After the VSSA-CFW processing, the VSSA-CFW image was formed based on $S_{VSSA-CFW}$ in (7) by envelope detection and logarithmic compression.

$$\mathrm{Wt}_{\mathrm{CF}}(\mathrm{t})=\frac{\left|\sum_{\mathrm{i}=00}^{\mathrm{N}-1}\mathrm{RF}(\mathrm{i},,\mathrm{t}-\Delta\mathrm{t}_{\mathrm{i}})\right|^{2}}{\mathrm{N}\sum_{\mathrm{i}=00}^{\mathrm{N}-1}\left|\mathrm{RF}(\mathrm{i},,\mathrm{t}-\Delta\mathrm{t}_{\mathrm{i}})\right|^{2}} \quad (6)$$

$$S_{VSSA-CFW}(t)=S_{VSSA}\,\mathrm{Wt}_{\mathrm{CF}}(\mathrm{t}) \quad (7)$$

B. Simulations in Field II

To assess the efficacy of the proposed method for IVUS imaging, simulations were conducted using Field II, an acoustic simulation tool based on Matlab [34]. Both linear and

rotational scan imaging were simulated to fully investigate the performance of the method for IVUS imaging. We first defined a 40MHz IVUS transducer with a flat 0.5mm×0.5mm aperture to match the transducer that we used in the experiments. Then we defined two types of phantoms: 5 point targets with 1mm axial separation and 0.25mm lateral separation were defined for lateral scan simulation; 5 point targets with 1mm axial separation and 60° angular separation counterclockwise were defined for rotational scan simulation. RF signals were acquired by updating phantom locations according to the lateral or rotational scanning paths. The step size is 3.6μm and 0.36° for the linear scan and rotational scan, respectively. VSSA focusing and CFW method mentioned above were applied to the simulated RF signals. After processing, VSSA-Only and VSSA-CFW images were formed by envelope detection and logarithmic compression. Lateral resolution at different depths of Raw, VSSA-Only, VSSA-CFW images was measured to quantify the effect of the proposed method on the lateral resolution. Image resolutions were determined by the −6dB beamwidth of the envelope signals from wire targets at different depths.

C. In Vitro Phantom and Ex Vivo Artery Imaging

Imaging data were acquired from phantoms and *ex vivo* human arteries to validate the performance of VSSA-CFW. We fabricated two wire phantoms of different distribution geometries (linearly separated and circularly separated) using 5 pieces of 10 um tungsten wire to study the resolution improvement for the linear and rotational scan. In the linearly separated wire phantom, the five pieces of wire are separated by 0.2mm and 1mm in lateral and axial direction, respectively. In the circularly separated wire phantom, the wires are separated by 60° and 1mm along angular (counterclockwise) and axial direction, respectively. Wire phantom images were acquired by linearly and rotationally scanning the IVUS transducer within the deionized water. The lateral and axial resolutions were measured in the same way as that for simulated images. A cylindrical agar based tissue-mimicking phantom with 3mm diameter lumen in the center was fabricated to investigate the improvement in imaging depth. During imaging, the central lumen was filled with deionized water. Imaging depth was determined as the depth where signal-to-noise ratio (SNR) falls below 6dB. For *ex vivo* imaging, a section of human cadaver artery sample was fixed coaxially using congealed agar solution within a 30mL beaker. During imaging, the beaker was mounted onto a rotary motor to obtain the cross-sectional image.

To evaluate the improvements on CNR quantitatively, two cylindrical agar-based anechoic cyst phantoms with 3mm diameter lumen in the center were fabricated. One holds three cysts of 1mm in diameter located at 2mm, 3mm and 4mm away from lumen center. The other phantom has 3 cysts of 0.5mm, 1mm and 2mm in diameter located at 2mm away from the center of lumen [37]. During imaging, both the central lumen and cyst lumens were filled with deionized water. The CNR was computed for each of cysts within the phantom using a 50dB dynamic range. CNR was defined by (8)[38, 39]:

$$CNR=\frac{|\mu_c-\mu_b|}{\sqrt{(\sigma_c^2+\sigma_b^2)}}, \quad (8)$$

where μ_c and μ_b is the mean intensity values (in decibels) within the cyst region and background region, respectively. σ_c and σ_b is the standard deviation of cyst and background region, respectively. In this situation, the background region was the tissue-mimicking agar phantom region.

A 40MHz side-looking miniature IVUS transducer of 1 mm in outer diameter and 0.5mm×0.5mm aperture size was used to acquire images. The simulated beam profile of the transducer is shown in Fig. 1(a), where the narrowest beamwidth is achieved near the natural focus (1.7mm). Beam diverges at the off-focus region. During linear scanning, the transducer was mounted on a linear stage with the transducer aperture facing towards the wires within the water bath. 1000 scan lines were acquired with a 3.6μm step size to form the wire phantom image. During rotational scanning, the transducer tip remained stationary within the water-filled lumen of the imaged sample (wire phantom, agar phantom, and human artery) and cross-sectional images were achieved by rotating the sample using an integrated servo motor (Moog Animatics, Milpitas, CA, USA) [40]. 1000 scan lines were acquired with a 0.36° angular step size corresponding to around $\lambda/12$ step size at the transducer surface to ensure enough beam overlap between adjacent scan lines. A JSR DPR500 pulser/receiver was used to drive the transducer, receive, and amplify the RF signals. The amplified RF signals were digitized by a 12-bit digitizer (Gage Applied Technologies, Lockport, IL) at a sampling rate of 500MHz. The motor rotation and RF data acquisition were synchronized by a function generator to ensure acquiring 1000 scan lines per rotation of the motor. A custom-developed LabVIEW program (National Instruments, Austin, TX) was used to control the imaging procedure and save the raw RF data for offline processing and image display.

III. Results

The in vitro phantom imaging and ex vivo human artery imaging results demonstrate that the beamforming method VSSA-CFW can improve the image quality of single-element based IVUS imaging by improving the lateral resolution, extending imaging depth, and enhancing CNR.

A. Lateral Scan

Fig. 3 and Fig. 4 show images acquired by a linear scan in simulation and in the experiment, respectively. In the simulation results and experimental results, there is obvious resolution enhancement in the beamformed images across the whole imaging range, compared to the raw images. VSSA focusing decreases the mainlobe width and therefore an almost depth-independent lateral resolution is obtained, as indicated in Fig. 5. But the sidelobe level becomes higher, as shown in the VSSA-Only images in Fig. 3 and Fig. 4. After applying CFW onto the VSSA focused beam, the sidelobes are effectively suppressed and lateral resolution gets further improved. The lateral resolution was enhanced from 165–524 μm to 126–143μm after VSSA-CFW processing. The beam profile of wire phantom was plotted in Fig. 9(a) to better illustrate changes throughout the image processing procedure. Mainlobe width was narrowed after VSSA focusing, but accompanied with more obvious sidelobe. After VSSA-CFW processing, the side lobe was lowered and main lobe width is further

narrowed. For instance, sidelobe level was reduced by 34dB and resolution increased by 97μm for the simulated point target at 3.8mm after applying the CFW. The axial resolution for both simulation and experimental images maintains after processing. Different from the simulated results, cosmic tail artifact can be observed in experimental VSSA-Only and VSSA-CFW image in Fig. 4, which is caused by the ringing tail of the real transducer response. This artifact can be potentially removed by improving the transducer property.

B. Rotational Scan

The simulation results in Fig. 6 and experiment results in Fig. 7 of rotational scanning also show an increase in the lateral resolution over the whole imaged range. The resolution results are summarized in Fig. 8. Different from the linear scan mode, the VSSA-focusing alone does not improve the resolution of rotational scan mode since the moderate expansion of the synthesized aperture cannot compensate the beam divergence. However, after applying CFW, the lateral resolutions increase by up to 42% for both simulation and experimental results. As shown in Fig. 9(b), the beam profile f the wire phantom clearly shows the improvement after VSSA-CFW processing. For instance, 11dB sidelobe suppression and 2.5 degree resolution increase were obtained for the simulated point target at 3.5mm after CFW. Similar to the linear scan case, the axial resolution maintains after applying the VSSA-CFW.

From Fig. 9(a), it can also be found that the noise level is suppressed while the resolution is improved. This is because of the noise-suppressing nature of the VSSA-CFW beamforming method, which is capable of removing random non-coherent signals while enhancing the coherent signals. Owing to the decrease in noise floor, the imaging depth was improved from 4.7mm to 6.5mm after applying VSSA-CFW through the in vitro measurement on the agar-based tissue-mimicking phantom.

The experimental result of agar-based anechoic cyst phantom imaging is shown in Fig. 10. The calculated CNR values are summarized in Fig. 11. The CNR improves after applying VSSA. However, the higher side lobe still creates artifacts within the cyst region. After applying CFW onto the VSSA focused image, the CNR further improves, which demonstrates that CFW can effectively suppress the sidelobes and result in a higher CNR for cyst of different sizes and at different depths. In the VSSA-CFW image, superior CNR can be observed through the more distinct boundary between anechoic area and surrounding agar phantom, as well as at the boundary of the central lumen.

IVUS images of the human artery are shown in Fig. 12. The suppressed noise floor and enhanced resolution help to better delineate media layer structure of the artery wall, as indicated by the yellow arrowheads.

IV. Discussion and Conclusion

This study demonstrates that the beamforming method of combining virtual source synthetic aperture and coherence factor weighting can effectively improve the overall quality of IVUS images, including lateral resolution, imaging depth and CNR. This is for the first time, to our best knowledge, that the VSSA-CFW is applied to single-element based IVUS imaging.

In this application, the natural focal point of the transducer is treated as a virtual source based on which the synthetic aperture processing is performed. In the linear scan mode, VSSA focusing improves the lateral resolution by synthesizing a large aperture. However, this aperture synthesis procedure brings in high sidelobe level. CFW is therefore needed to reduce the sidelobe level since it can modulate the image intensity according to the coherence of the delayed RF signals. For a point target, the coherence factor is highest along the synthesized beam axis that passes through the point target, since the scan lines are highly coherent after focusing delay. However, for the synthesized beam that's off the point target, the coherence factor will be decreased because of the steering error for focusing delay calculation. Coherence factor peaks at the center of point target (center of the mainlobe) and decreases with increasing distance to the center of the point target. The image intensity from directions other than the central synthesized beam will be suppressed. Therefore, CFW can effectively lower the sidelobes and improve the lateral resolution. In the rotational scan mode, VSSA focusing alone cannot improve the resolution because of the rotation geometry. The synthesized aperture size increases linearly with increasing depth under linear scan mode. Under rotational scan mode, the synthesized aperture size is not large enough to compensate the broadening of the beam pattern. As imaging depth increases, the synthesized aperture only experiences moderate expansion [29] [41]. However, after applying CFW, the lateral resolution and CNR still get obvious improvement. Therefore, VSSA-CFW can improve lateral resolution for both linear and rotational scan at all depths beyond the natural focal region, where the most meaningful clinical information potentially lies.

The summation procedure of VSSA-CFW inherently increases the image signal-to-noise ratio (SNR) and consequently extends the imaging depth. A 1.8mm imaging depth extension was obtained for the agar-based phantom. Higher image SNR also enables the adoption of a higher frequency transducer to achieve higher resolution without sacrificing the penetration depth.

The VSSA-CFW beamforming method holds a promising potential for clinical translation. It can be integrated into the current commercial IVUS imaging system readily to postprocess the acquired IVUS imaging data. Several future works need to be done to translate this technique to the clinic. First of all, the effect of non-uniform rotation distortion (NURD) on VSSA-CFW should be evaluated since NURD is one of the main issues in current IVUS image. We have run the simulation in Field II for anechoic cyst phantom imaging with three different types of NURD (Random error angle, Sinusoidal modulation, Kinking). According to the imaging result in Fig. 13, VSSA-CFW can still perform well under moderate random or periodic error, and outside the kinking region. Contrast-to-noise ratio gets improved for cyst of different sizes and locations under NURD. CNR for the 2mm cyst is listed in Fig. 13 to illustrate the improvement.

The performance of VSSA-CFW on *in vivo* imaging data also needs to be investigated to further validate this technique. Besides the NURD, the motion of blood vessel and imaging catheter during *in vivo* imaging can affect the performance of VSSA-CFW. The synthetic aperture method is subject to motion artifact. Unwanted image artifacts can arise if the movement of imaged target is more than $\lambda/4$ during the time period needed to receive all the scanlines needed for aperture synthesis [42]. By increasing the imaging speed (higher pulse

repetition frequency and higher scanning speed) and adopting motion compensation procedures, the motion artifact problem is supposed to be solved and will not degrade the performance significantly. We also need to validate the VSSA-CFW method on the 3D imaging data acquired under rotational pullback motion, during which the acquired RF signal corresponds to both rotational and linear position shift. Last but not least, statistical studies about the improvement of the method on different types of plaques need to be performed to further validate the efficacy of the image processing method.

In summary, VSSA-CFW can effectively improve image quality in both cross-sectional and longitudinal plane beyond the natural focal point, which ensures the full coverage of the region of interest for vessels of different sizes. What's more, it can also be applied to intravascular photoacoustic imaging, for which lower noise level and better lateral resolution are highly desired [28]. The improvement in image quality will also be a benefit for those increasingly miniaturized IVUS transducers, which is indispensable for advancing current multi-modality intravascular imaging techniques. IVUS images with improved lateral resolution, extended imaging depth, and enhanced CNR in both cross-sectional and longitudinal view can assist cardiologists to acquire more accurate plaque volume measurement, layer structure delineation, and artery remodeling evaluation.

Acknowledgments

The authors acknowledge Dr. Chi Tat Chiu for helping with PZFlex simulation. The authors also thank the individuals who donate their bodies and tissues for the advancement of education and research.

References

1. Mozaffarian D, Benjamin EJ, et al. M. Writing Group. Executive Summary: Heart Disease and Stroke Statistics–2016 Update: A Report From the American Heart Association. Circulation. Jan 26; 2016 133(4):447–54. [PubMed: 26811276]
2. Oesterle SN, Limpijankit T, Yeung AC, et al. Ultrasound logic: the value of intracoronary imaging for the interventionist. Catheter Cardiovasc Interv. Aug; 1999 47(4):475–90. [PubMed: 10470481]
3. Virmani R, Burke AP, Kolodgie FD, et al. Pathology of the thin-cap fibroatheroma: a type of vulnerable plaque. J Interv Cardiol. Jun; 2003 16(3):267–72. [PubMed: 12800406]
4. Li J, Li X, Mohar D, et al. Integrated IVUS-OCT for real-time imaging of coronary atherosclerosis. JACC Cardiovasc Imaging. Jan; 2014 7(1):101–3. [PubMed: 24433713]
5. Li J, Ma T, Mohar D, et al. Ultrafast optical-ultrasonic system and miniaturized catheter for imaging and characterizing atherosclerotic plaques in vivo. Sci Rep. 2015; 5:18406. [PubMed: 26678300]
6. Rieber J, Meissner O, Babaryka G, et al. Diagnostic accuracy of optical coherence tomography and intravascular ultrasound for the detection and characterization of atherosclerotic plaque composition in ex-vivo coronary specimens: a comparison with histology. Coron Artery Dis. Aug; 2006 17(5): 425–30. [PubMed: 16845250]
7. Ma T, Yu M, Li J, et al. Multi-frequency intravascular ultrasound (IVUS) imaging. IEEE Trans Ultrason Ferroelectr Freq Control. Jan; 2015 62(1):97–107. [PubMed: 25585394]
8. Ma J, Martin HK, Li Y, et al. Design factors of intravascular dual frequency transducers for super-harmonic contrast imaging and acoustic angiography. Phys Med Biol. May 7; 2015 60(9):3441–57. [PubMed: 25856384]
9. Schultz CJ, Serruys PW, van der Ent M, et al. First-in-man clinical use of combined near-infrared spectroscopy and intravascular ultrasound: a potential key to predict distal embolization and no-reflow? J Am Coll Cardiol. Jul 20.2010 56(4):314. [PubMed: 20633824]
10. Brugaletta S, Sabaté M. Assessment of Plaque Composition by Intravascular Ultrasound and Near-Infrared Spectroscopy. Circulation. 2014; 78(7):1531–1539.

11. Wang P, Ma T, Slipchenko MN, et al. High-speed intravascular photoacoustic imaging of lipid-laden atherosclerotic plaque enabled by a 2-kHz barium nitrite raman laser. Sci Rep. 2014; 4:6889. [PubMed: 25366991]
12. Piao Z, Ma T, Li J, et al. High speed intravascular photoacoustic imaging with fast optical parametric oscillator laser at 1.7 mum. Appl Phys Lett. Aug 24.2015 107(8):083701. [PubMed: 26339072]
13. Liang S, Ma T, Jing J, et al. Trimodality imaging system and intravascular endoscopic probe: combined optical coherence tomography, fluorescence imaging and ultrasound imaging. Opt Lett. Dec 1; 2014 39(23):6652–5. [PubMed: 25490644]
14. Ma T, Zhou B, Hsiai TK, et al. A Review of Intravascular Ultrasound-based Multimodal Intravascular Imaging: The Synergistic Approach to Characterizing Vulnerable Plaques. Ultrason Imaging. Sep; 2016 38(5):314–31. [PubMed: 26400676]
15. Ma J, Martin KH, Dayton PA, et al. A preliminary engineering design of intravascular dual-frequency transducers for contrast-enhanced acoustic angiography and molecular imaging. IEEE Trans Ultrason Ferroelectr Freq Control. 2014; 61(5):870–880. [PubMed: 24801226]
16. Li Y, Ma J, Martin K, et al. An Integrated System for Super-Harmonic Contrast-Enhanced Ultrasound Imaging: Design and Intravascular Phantom Imaging Study. IEEE Trans Biomed Eng. Sep; 2016 63(9):1933–1943. [PubMed: 26672030]
17. Maresca D, Adams S, Maresca B, et al. Mapping intravascular ultrasound controversies in interventional cardiology practice. PLoS One. 2014; 9(5):e97215. [PubMed: 24816741]
18. Syed MA, Hodgson JM. Enhanced IVUS: Advances Allowing Higher Resolution and Integrated Devices. Current Cardiovascular Imaging Reports. 2016; 9(8)
19. Lee J, Jang J, Chang JH. Oblong-Shaped Focused Transducers for Intravascular Ultrasound Imaging. IEEE Trans Biomed Eng. May; 2016 64(3):671–680. [PubMed: 27244714]
20. Passmann C, Ermert H. A 100-MHz ultrasound imaging system for dermatologic and ophthalmologic diagnostics. IEEE Trans Ultrason Ferroelectr Freq Control. Jul; 1996 43(4):545–552.
21. Frazier CH, O'Brien WR. Synthetic aperture techniques with a virtual source element. IEEE Trans Ultrason Ferroelectr Freq Control. 1998; 45(1):196–207. [PubMed: 18244172]
22. Bae MH, Jeong MK. A study of synthetic-aperture imaging with virtual source elements in B-mode ultrasound imaging systems. IEEE Trans Ultrason Ferroelectr Freq Control. 2000; 47(6): 1510–9. [PubMed: 18238697]
23. Nikolov SI, Jensen JA. Virtual ultrasound sources in high-resolution ultrasound imaging. Medical Image 2002: Ultrasonic Imaging and Signal Processing. 2002; 4687:395–405.
24. Kortbek J, Jensen JA, Gammelmark KL. Sequential beam-forming for synthetic aperture imaging. Ultrasonics. Jan; 2013 53(1):1–16. [PubMed: 22809678]
25. Hansen PM, Hemmsen M, Brandt A, et al. Clinical evaluation of synthetic aperture sequential beamforming ultrasound in patients with liver tumors. Ultrasound Med Biol. Dec; 2014 40(12): 2805–10. [PubMed: 25308936]
26. Hemmsen MC, Rasmussen JH, Jensen JA. Tissue harmonic synthetic aperture ultrasound imaging. J Acoust Soc Am. Oct; 2014 136(4):2050–6. [PubMed: 25324103]
27. Di Ianni, T., Hemmsen, MC., Jensen, JA. Vector Velocity Estimation for Portable Ultrasound using Directional Transverse Oscillation and Synthetic Aperture Sequential Beamforming. 2016 IEEE International Ultrasonics Symposium (Ius); 2016.
28. Liao CK, Li ML, Li PC. Optoacoustic imaging with synthetic aperture focusing and coherence weighting. Opt Lett. Nov 1; 2004 29(21):2506–8. [PubMed: 15584276]
29. Kortbek, J., Jensen, JA., Gammelmark, KL. Synthetic aperture focusing applied to imaging using a rotating single element transducer. 2007 IEEE Ultrasonics Symposium Proceedings; 2007. p. 1504-1507.
30. Karaman M, Li PC, Odonnell M. Synthetic-Aperture Imaging for Small-Scale Systems. IEEE Trans Ultrason Ferroelectr Freq Control. May; 1995 42(3):429–442.
31. Mallart R, Fink M. Adaptive Focusing in Scattering Media through Sound-Speed Inhomogeneities - the Vancittert-Zernike Approach and Focusing Criterion. J Acoust Soc Am. Dec; 1994 96(6): 3721–3732.

32. Hollman, KW., Rigby, KW., O'Donnell, M. Coherence factor of speckle from a multi-row probe. 1999 IEEE Ultrasonics Symposium Proceedings; 1999. p. 1257-1260.
33. Li ML, Guan WJ, Li PC. Improved synthetic aperture focusing technique with applications in high-frequency ultrasound imaging. IEEE Trans Ultrason Ferroelectr Freq Control. Jan; 2004 51(1):63–70. [PubMed: 14995017]
34. Jensen JA, Svendsen NB. Calculation of pressure fields from arbitrarily shaped, apodized, and excited ultrasound transducers. IEEE Trans Ultrason Ferroelectr Freq Control. 1992; 39(2):262–7. [PubMed: 18263145]
35. Li ML, Zhang HE, Maslov K, et al. Improved in vivo photoacoustic microscopy based on a virtual-detector concept. Opt Lett. Feb 15; 2006 31(4):474–6. [PubMed: 16496891]
36. Li PC, Li ML. Adaptive imaging using the generalized coherence factor. IEEE Trans Ultrason Ferroelectr Freq Control. Feb; 2003 50(2):128–141. [PubMed: 12625586]
37. Turnbull DH, Lum PK, Kerr AT, et al. Simulation of B-scan images from two-dimensional transducer arrays: Part I–Methods and quantitative contrast measurements. Ultrason Imaging. Oct; 1992 14(4):323–43. [PubMed: 1296337]
38. Kim C, Yoon C, Park JH, et al. Evaluation of Ultrasound Synthetic Aperture Imaging Using Bidirectional Pixel-Based Focusing: Preliminary Phantom and In Vivo Breast Study. IEEE Trans Biomed Eng. Oct; 2013 60(10):2716–2724. [PubMed: 23686939]
39. Moghimirad E, Hoyos CAV, Mahloojifar A, et al. Synthetic Aperture Ultrasound Fourier Beamformation Using Virtual Sources. IEEE Trans Ultrason Ferroelectr Freq Control. Dec; 2016 63(12):2018–2030. [PubMed: 27623581]
40. Li X, Wu W, Chung Y, et al. 80-MHz Intravascular Ultrasound Transducer Using PMN-PT Free-Standing Film. IEEE Trans Ultrason Ferroelectr Freq Control. Nov; 2011 58(11):2281–2288. [PubMed: 22083761]
41. Andresen H, Nikolov SI, Pedersen MM, et al. Three-Dimensional Synthetic Aperture Focusing Using a Rocking Convex Array Transducer. IEEE Trans Ultrason Ferroelectr Freq Control. May; 2010 57(5):1051–1063. [PubMed: 20442016]
42. O'Donnell M, Thomas LJ. Efficient synthetic aperture imaging from a circular aperture with possible application to catheter-based imaging. IEEE Trans Ultrason Ferroelectr Freq Control. 1992; 39(3):366–80. [PubMed: 18267647]

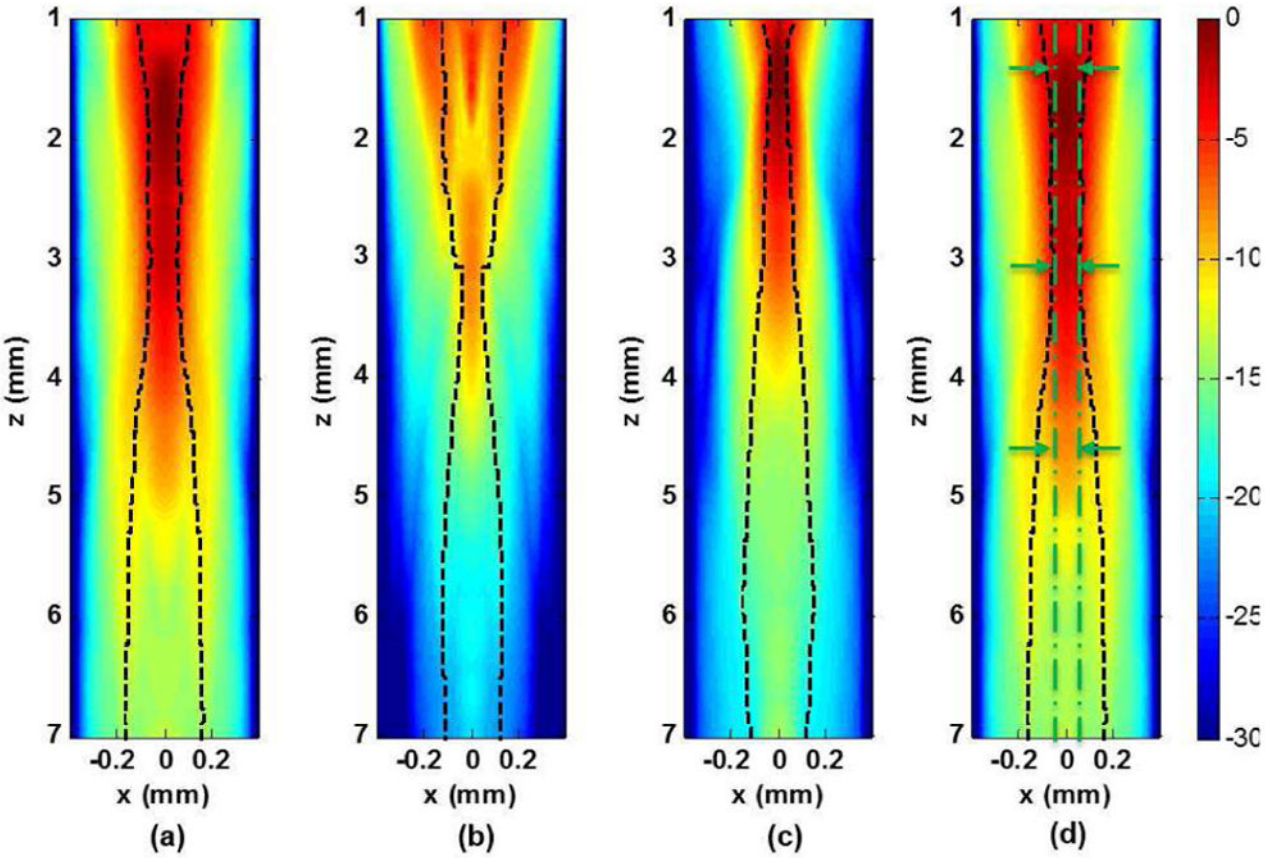

Fig. 1.

Simulated two-way beam patterns and −6dB beam width contour (black dashed line) of IVUS transducers with 0.5mm active aperture size: (a) 40MHz IVUS transducer with flat aperture, (b) 80MHz IVUS transducer with flat aperture, (c) 40MHz IVUS transducer with mechanical focusing at 3mm. (d) Simulated beam pattern from (a) with expected −6dB beamwidth contour (green dash dot line) after VSSA-CFW processing. The x-axis is lateral direction, and the z-axis is axial direction.

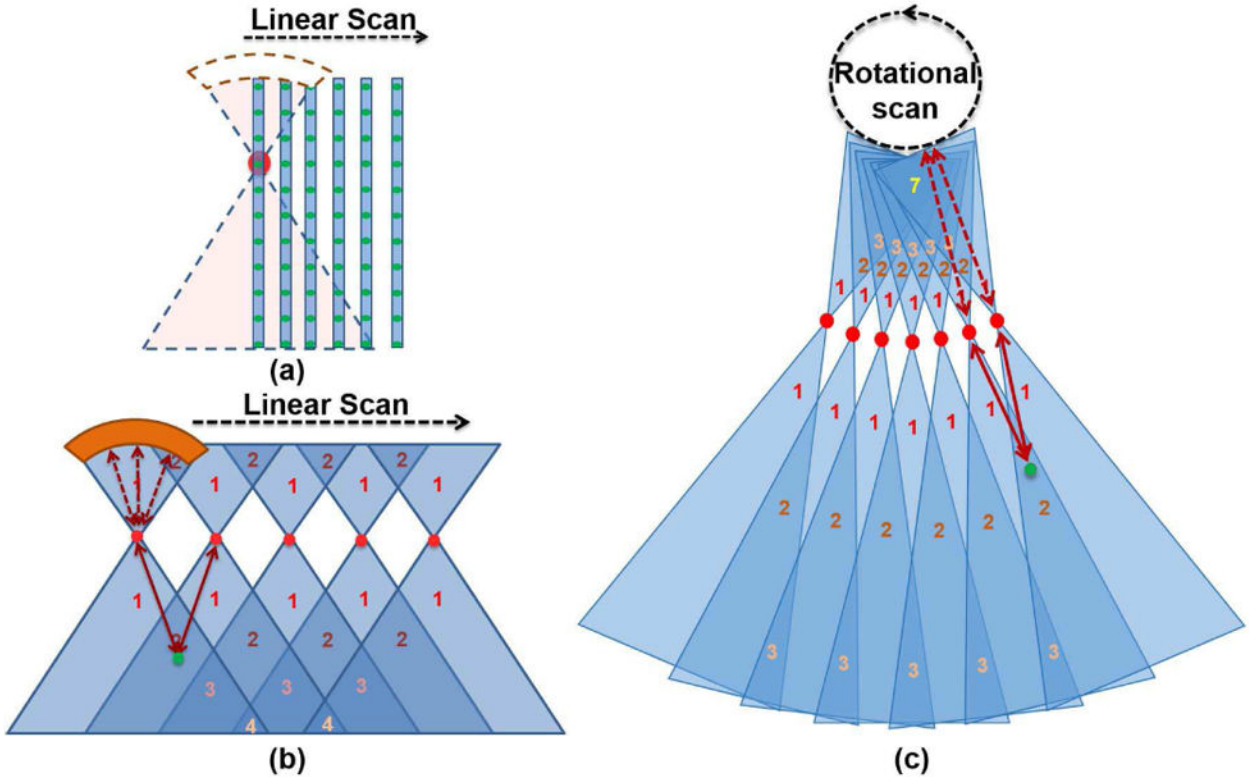

Fig. 2.

(a) Concept of traditional mechanical scan B-mode imaging, where the acoustic field of the transducer is shown in dashed line. The red dots denote the transmit focus. The green dots denote the imaging point. (b) Concept of virtual source synthetic imaging in linear scan mode. The number in the image shows the number of overlapping acoustic field. (c) Concept of virtual source synthetic imaging in rotational scan mode.

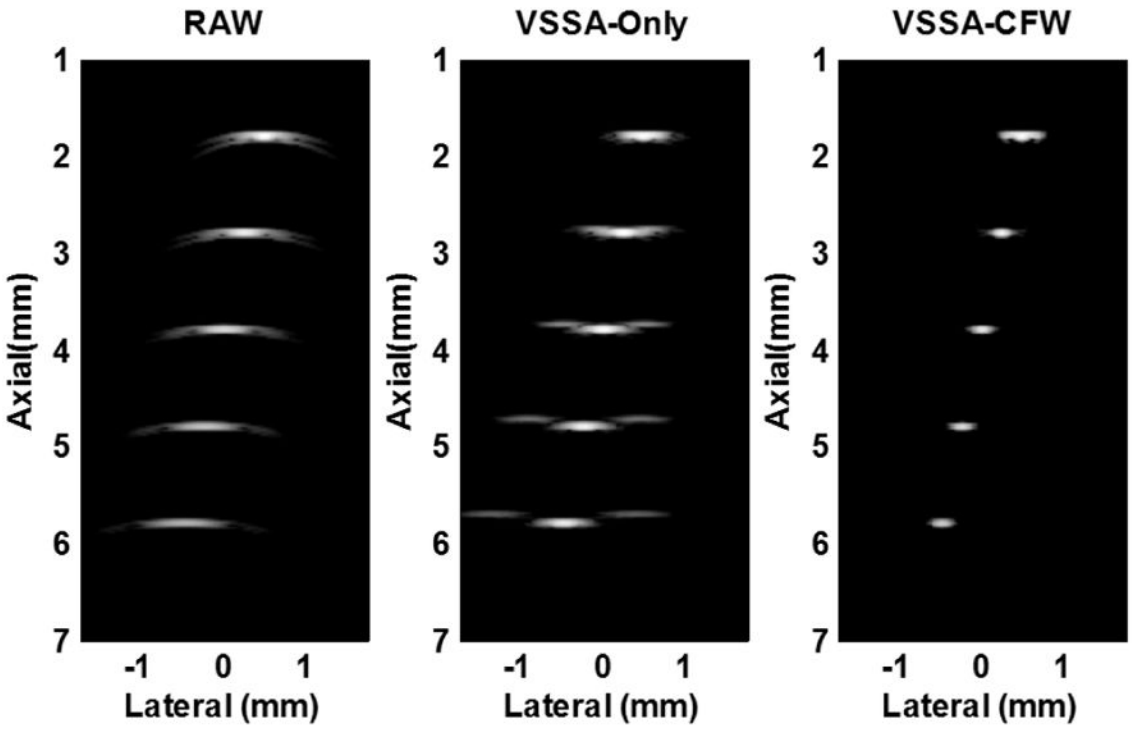

Fig. 3.
Simulation results of wire phantom imaging by linear scanning. Dynamic range: 50dB.

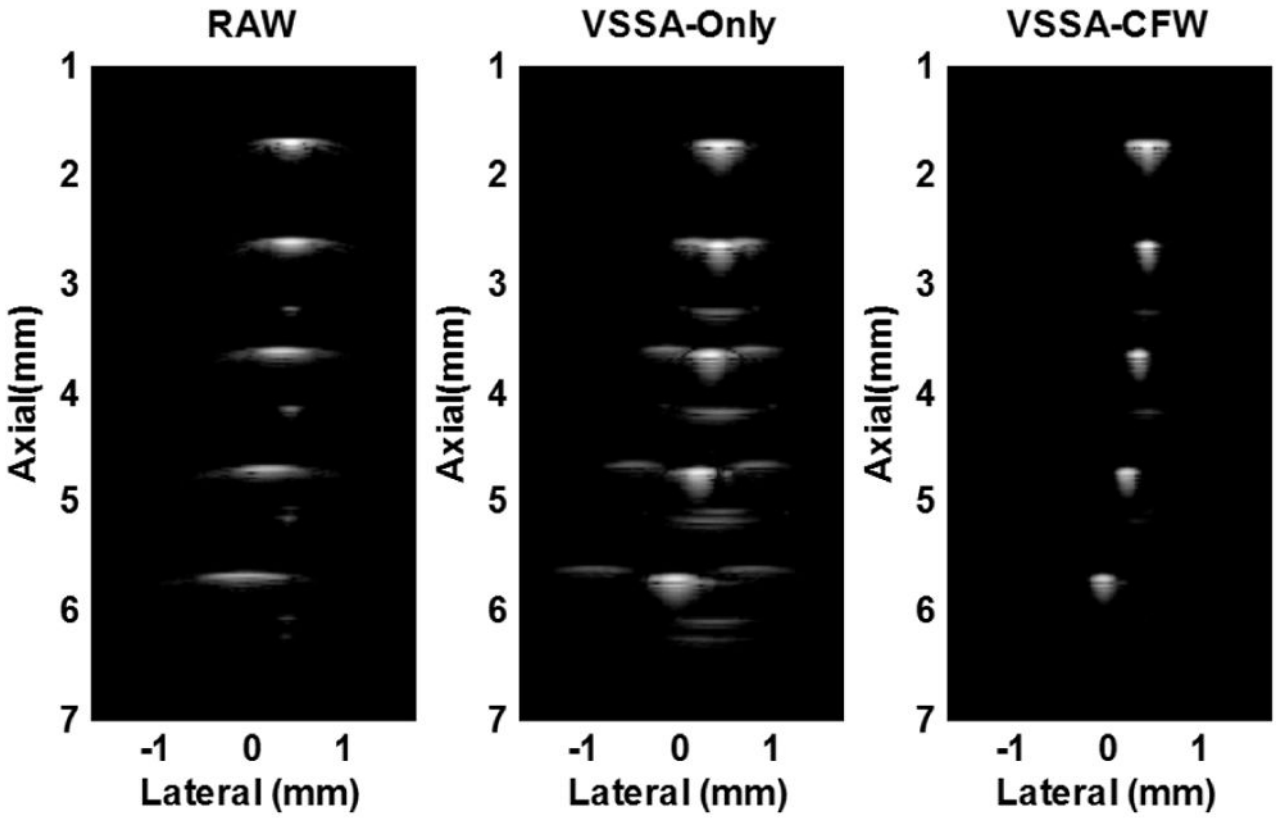

Fig. 4.
Experimental results of wire phantom imaging by linear scanning. Dynamic range: 50dB.

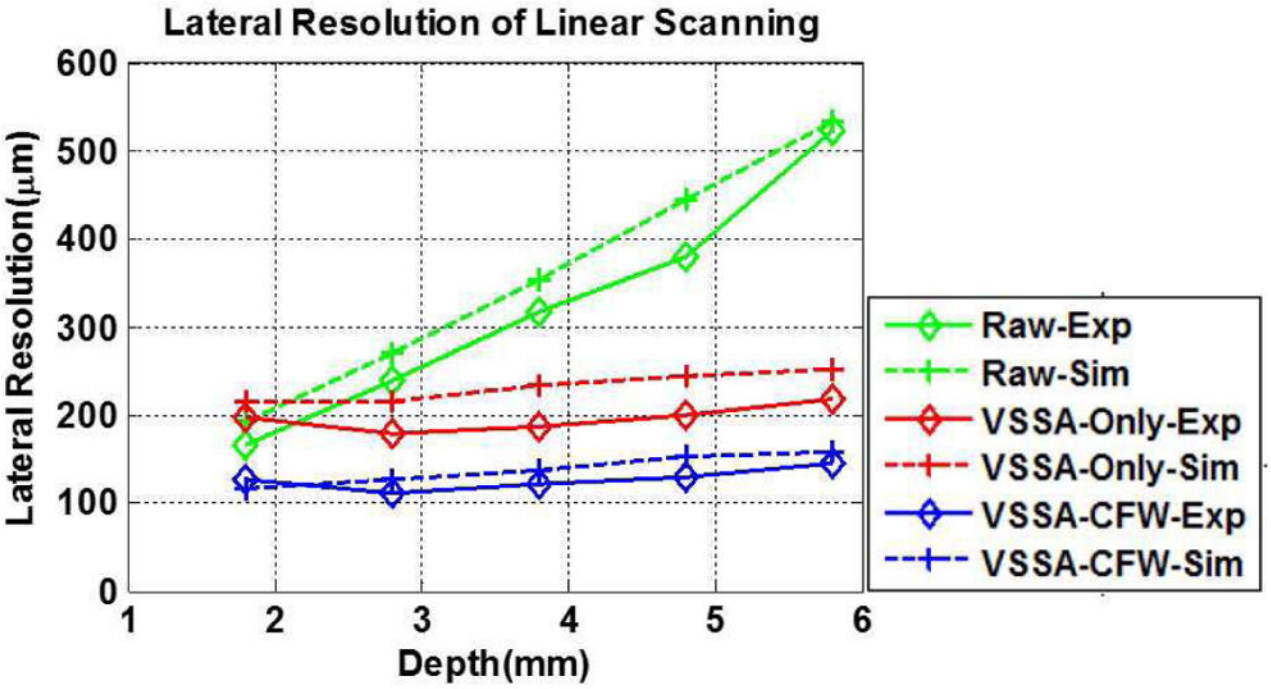

Fig. 5.

−6dB lateral resolution results of wire phantom images by linear scanning.

Fig. 6.
Simulation results of wire phantom imaging by rotational scanning. Dynamic Range: 50dB. Scale bar: 2mm.

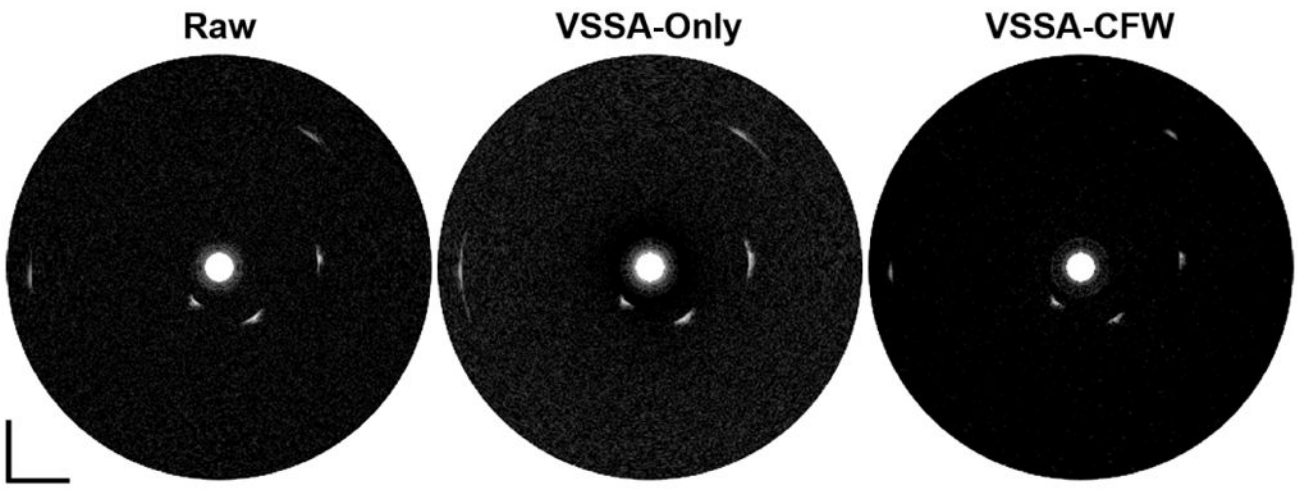

Fig. 7.

Experimental results of wire phantom imaging by rotational scanning. Dynamic Range: 50dB. Scale bar: 2mm.

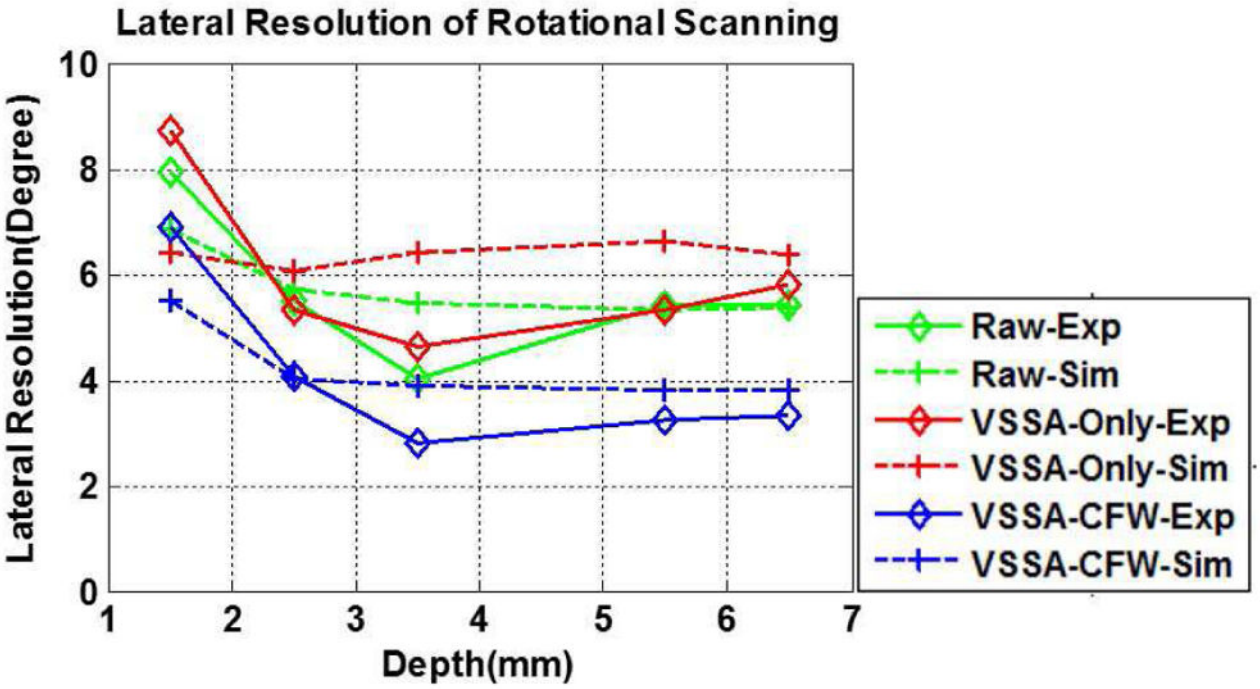

Fig. 8.

−6dB lateral resolution results of wire phantom images by rotational scanning.

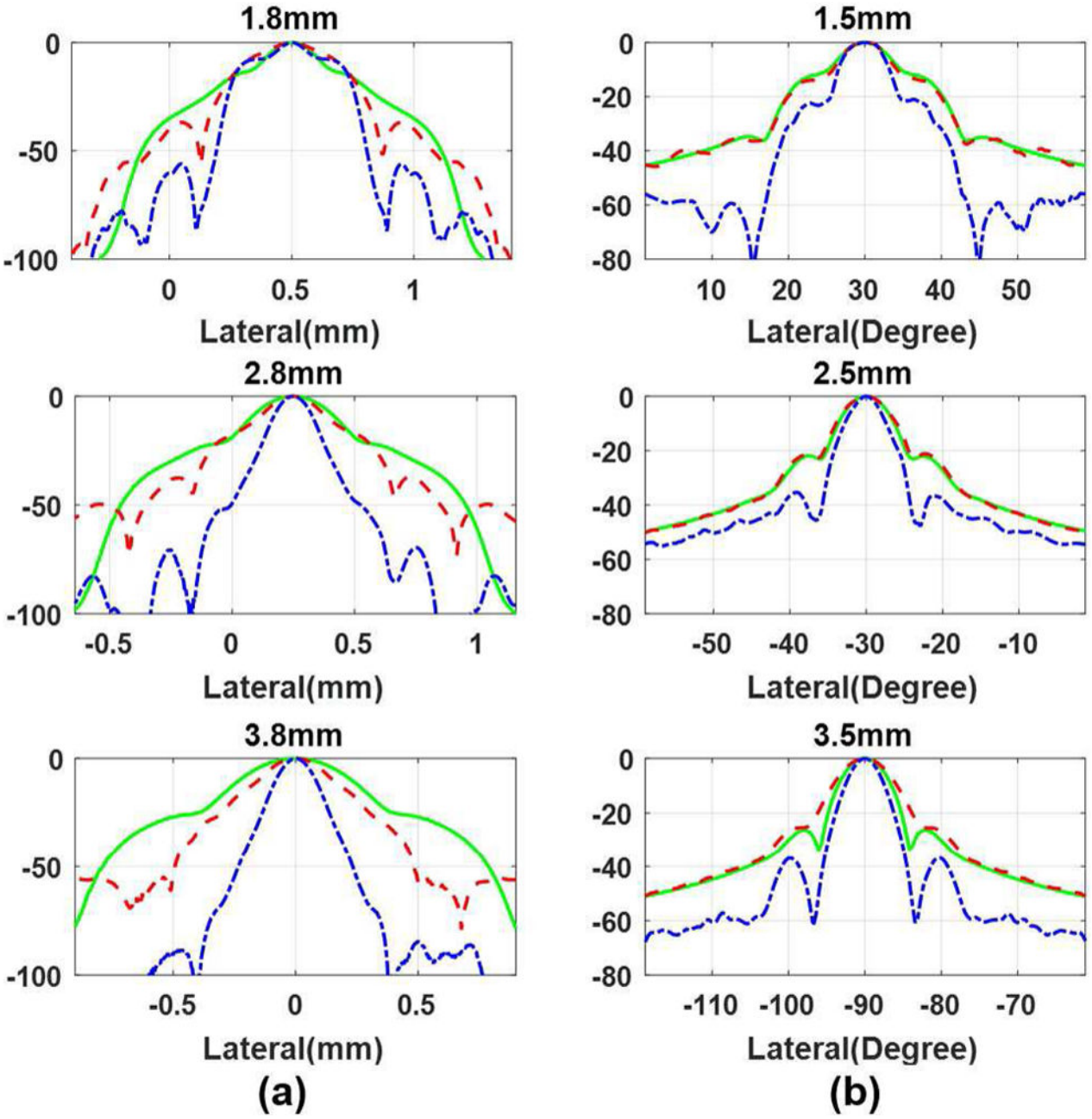

Fig. 9.

Lateral beam profiles of the simulated data for the two different scanning mode. (a) Linear Scanning; (b) Rotational scanning. Green solid line: Raw data. Red dashed line: VSSA-Only data. Blue dot dash line: VSSA-CFW.

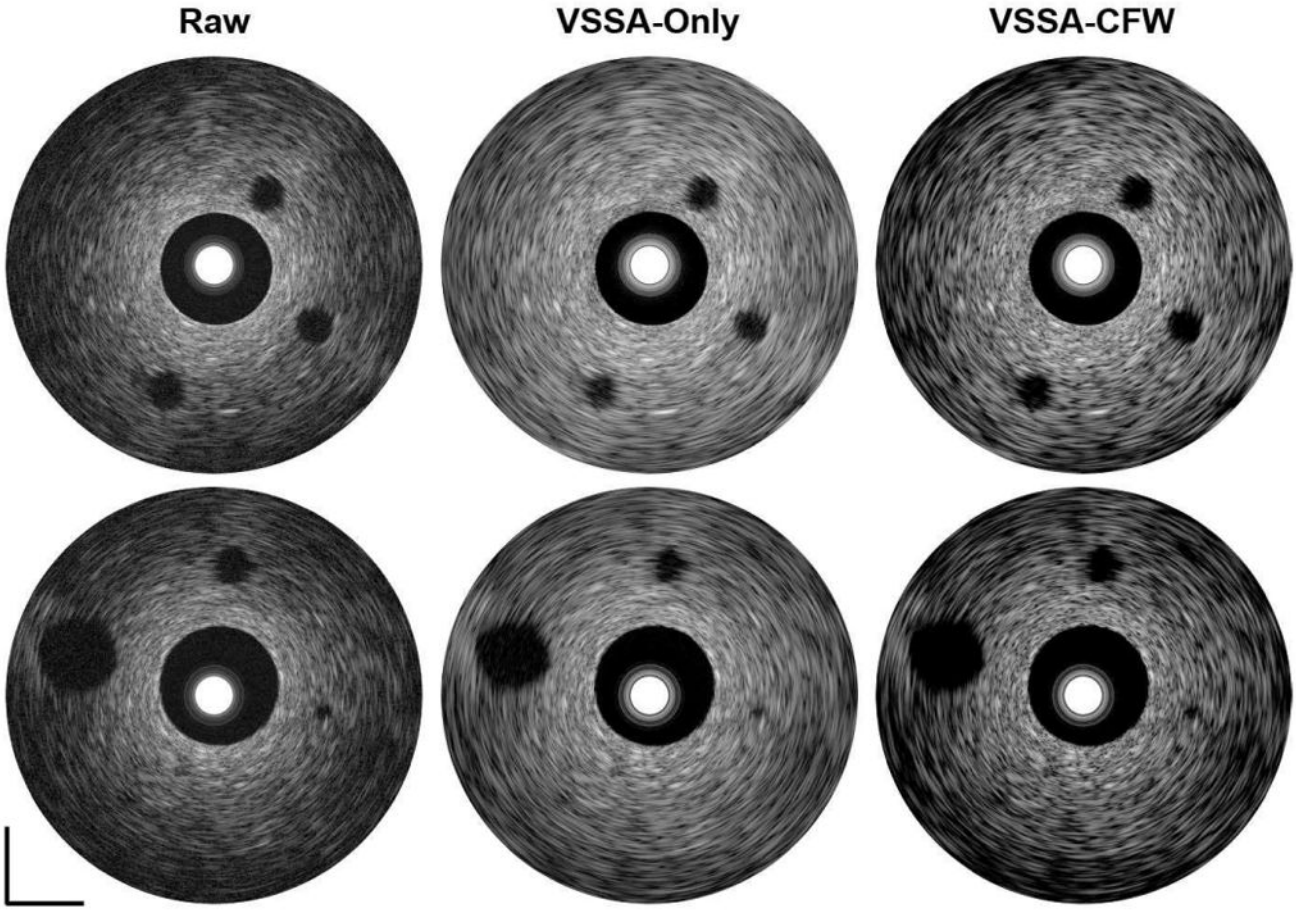

Fig. 10.

Experimental imaging results of the two agar-based anechoic cyst phantom imaging: top row shows phantom with 1mm cyst at different depth; bottom row shows phantom with different cysts at 3mm. Dynamic range: 50dB. Scale bar: 2mm.

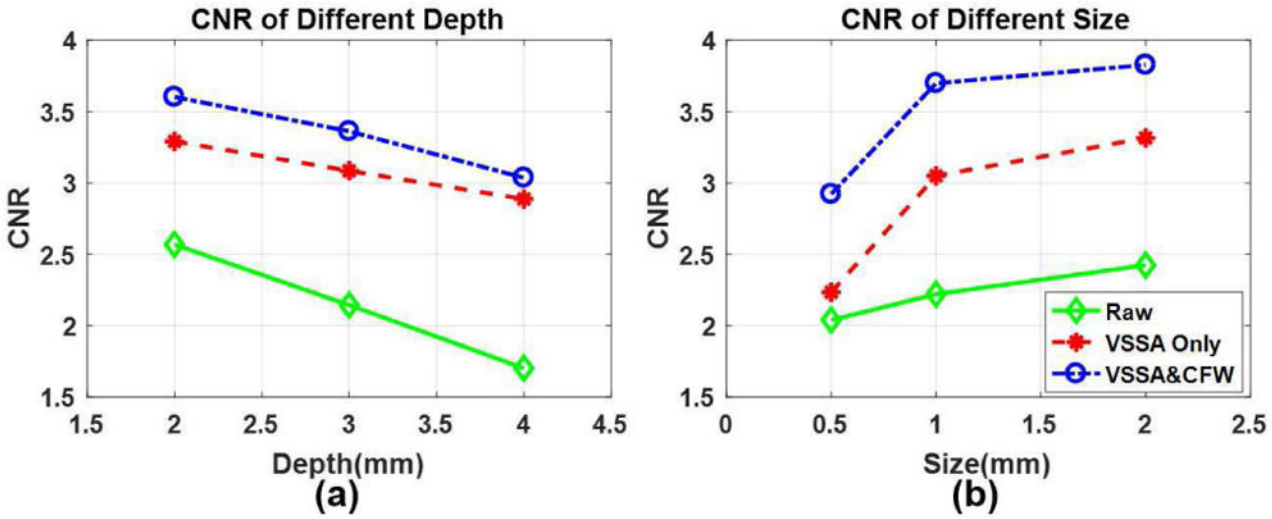

Fig. 11.

Contrast-to-noise ratio (CNR) results of the two anechoic cyst phantom images. (a) CNR of 1mm cyst at different depth. (b) CNR of different cysts at 3mm.

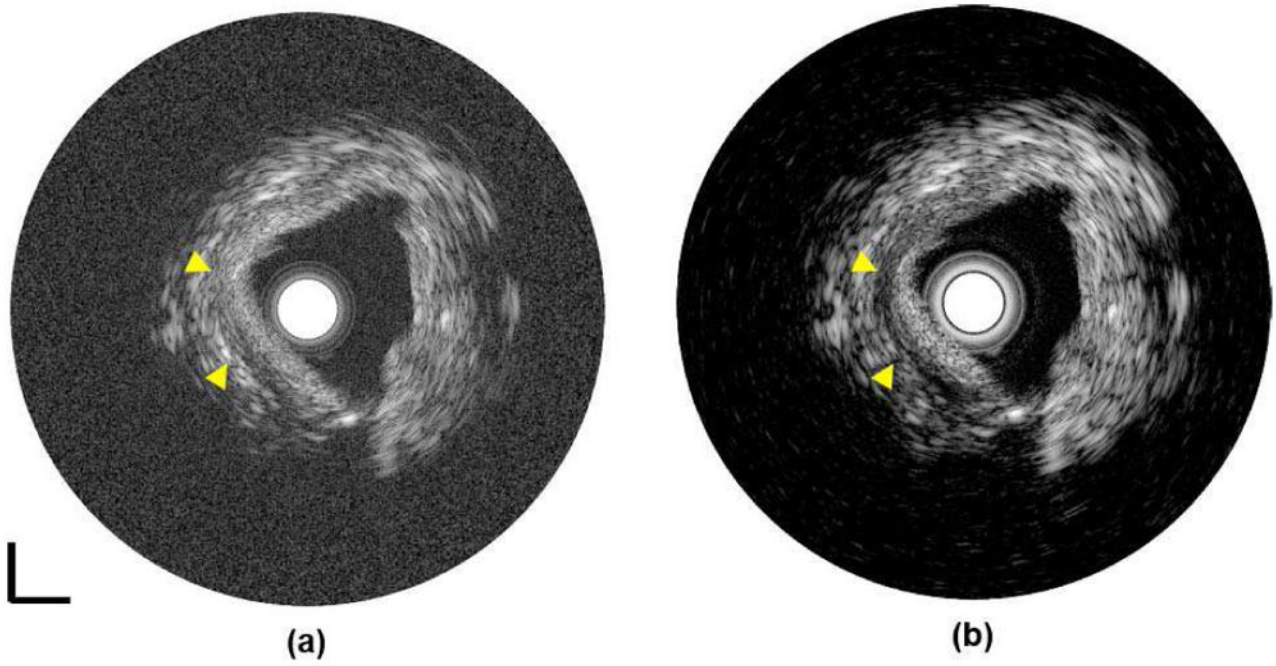

Fig. 12.

Experimental result of ex vivo human artery imaging: (a) Raw image, (b) Beamformed image using VSSA-CFW. Dynamic range: 50dB. Scale bar: 1mm;

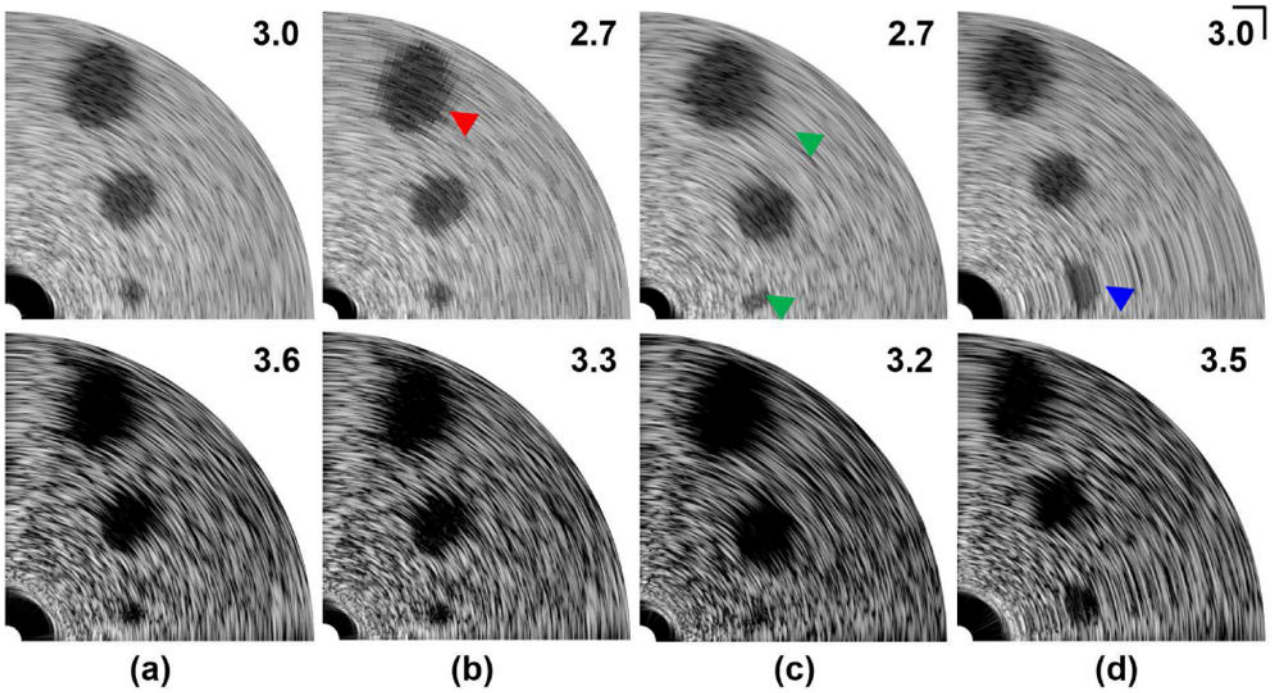

Fig. 13.

Simulated anechoic cyst phantom images with NURD. Top row shows Raw image and bottom row shows VSSA-CFW image: (a) Uniform rotation with 0.225° angular step size; (b) Rotation with random error angle within (−1.125°–1.125°); (c) Rotation with sinusoidal modulated error angle within (−0.0675°–0.0675°); (d) Rotation with kinking within 9° range. Arrowheads indicate the artifact from NURD. The number refers to the CNR value for the 2mm cyst. Dynamic range: 70dB. Scale bar: 1mm.